

Impact of intrinsic amorphous silicon bilayers in silicon heterojunction solar cells

Hitoshi Sai (齋均),^{1,2,a)} Po-Wei Chen (陳柏璋),^{1,3} Hung-Jung Hsu (許宏榮),¹ Takuya Matsui (松井卓矢),^{1,2} Shota Nunomura (布村正太),^{1,2} and Koji Matsubara (松原浩司)^{1,2}

¹Research Center for Photovoltaics, National Institute of Advanced Industrial Science and Technology (AIST), Tsukuba, Ibaraki 305-8568, Japan

²Renewable Energy Research Center, National Institute of Advanced Industrial Science and Technology (AIST), Koriyama, Fukushima 963-0298, Japan

³Department of Photonics, College of Electrical and Computer Engineering, National Chiao Tung University, Hsinchu 300, Taiwan

(Received 18 June 2018; accepted 21 August 2018; published online 11 September 2018)

The impact of intrinsic amorphous silicon bilayers in amorphous silicon/crystalline silicon (a-Si:H/c-Si) heterojunction solar cells is investigated. The microstructure factor R^* of the interfacial a-Si:H layer, which is related to the Si-H bond microstructure and determined by infrared absorption spectroscopy, is controlled in a wide range by varying the growth pressure and the power density in plasma-enhanced chemical vapor deposition process. Surface passivation at the a-Si:H/c-Si interface is significantly improved by using an intrinsic a-Si:H bilayer, i.e., a stack of an interfacial layer with a large R^* and an additional dense layer, particularly after the deposition of an overlying p-type a-Si:H layer. Consequently, the conversion efficiency of a-Si:H/c-Si heterojunction solar cells is markedly increased. However, it is also revealed that such an interfacial layer causes some negative effects including the increase in the series resistance and the current loss at the front side, depending on the growth condition. This result indicates that the interfacial layer has a significant impact on both the majority and the minority carrier transport. Thus, R^* of the interfacial layer is an important parameter for obtaining good surface passivation at the a-Si:c-Si interface, but not the sole parameter determining the conversion efficiency of a-Si:H/c-Si heterojunction solar cells.

Published by AIP Publishing. <https://doi.org/10.1063/1.5045155>

I. INTRODUCTION

Hydrogenated amorphous silicon (a-Si:H), which is often grown by plasma-enhanced chemical vapor deposition (PECVD) or hot-wire CVD (HWCVD), is intensively used in photovoltaic applications both in crystalline Si (c-Si)^{1,2} and thin-film Si solar cells.^{3,4} a-Si:H is known as one of the best materials for passivation of c-Si surfaces, and its high potential has been successfully demonstrated by very high $V_{OC} > 750$ mV (Refs. 5 and 6) and record efficiencies >25% in a-Si:H/c-Si heterojunction (SHJ) solar cells.^{7–10} Because of its excellent surface passivation capability, SHJ cells are suited to thinner c-Si wafers, in which surface recombination plays a more critical role.^{5,11–13} In addition, SHJ solar cells possess lower temperature coefficients than the conventional homo-junction c-Si cells, and therefore a higher energy yield is obtained in outdoor operation.^{14–16} Thus, SHJ solar cells are expected to expand their share in the photovoltaic industry in coming years.

Since the suppression of surface recombination is of prime importance in SHJ cells, the mechanism of surface passivation at the a-Si:H/c-Si interface has been actively investigated. It is widely known that the insertion of a thin intrinsic (i) layer between a c-Si wafer and an overlying doped layer is key to realizing good surface passivation.^{1,2,17} The growth

condition of the i-layer must be controlled carefully, since epitaxial growth at the a-Si:H/c-Si interface is known to be detrimental for surface passivation.^{18,19} For preventing such unwelcome epitaxial growth, interfacial layers such as very thin oxide,^{20,21} porous a-Si:H layers,^{22,23} and a-Si:H alloys such as amorphous silicon oxide and carbide (a-SiO_x:H^{24,25} and a-SiC_x:H²⁶) have been investigated. In addition, hydrogen plasma/radical treatment^{27–30} and hydrogen dilution of SiH₄ plasma^{31,32} have a significant impact on the surface passivation. It is widely known that surface passivation at the a-Si:H/c-Si interface is strongly affected also by overlying doped layers, which are necessary for electron or hole extraction.^{22,33,34} Recently, Liu *et al.* reported that use of underdense intrinsic a-Si:H layers is beneficial to obtain an improved V_{OC} after the deposition of a p-layer.²² In addition, Zhang *et al.* showed that an intrinsic a-Si:H bilayer with a porous interfacial layer improves the lifetime of SHJ cells,²³ though the detailed mechanism behind this is still not sufficiently clear. It should also be pointed out that a-Si:H plays multiple roles in SHJ cells not only as a surface passivation layer but also as a carrier transport channel to the electrode. Furthermore, the optical absorption loss caused by the a-Si:H layers must be minimized to increase the conversion efficiency.³⁵ However, the influence of such interfacial layers in SHJ cells on these aspects has not been fully understood yet.

In this paper, we investigate the impact of intrinsic a-Si:H bilayers and overlying p-layers in SHJ cells in a systematic

^{a)}E-mail: hitoshi-sai@aist.go.jp

way, mainly focusing on the first intrinsic layer which is directly grown on the c-Si surface. The optical properties and the Si-H bond microstructure in thin a-Si:H i-layers grown under different PECVD conditions are characterized by spectroscopic ellipsometry (SE) and Fourier transform infrared spectroscopy (FT-IR). These a-Si:H layers are applied to bilayer structures for passivating c-Si surfaces. The surface passivation capability of these bilayers and the effect of overlying p-layers are characterized by measuring minority carrier lifetimes. SHJ solar cells using these bilayers are also investigated in terms of not only surface passivation but also carrier collection and carrier transport.

II. EXPERIMENTAL

In this paper, we mainly focus on intrinsic bilayers on the p-side of SHJ solar cells, which are grown by 2-step PECVD process. The first i-layer (i_1) is grown with pure SiH₄ plasma under various conditions, while the second i-layer (i_2) is grown with hydrogen diluted plasma at a fixed condition.

For material characterization, a series of thin a-Si:H i-layers (~ 10 nm) were deposited on both sides of float-zone (FZ)-grown double-side polished wafers ($>1000\Omega\text{cm}$, $\langle 111 \rangle$ -oriented, 1-mm-thick) by means of PECVD, based on 13.56 MHz capacitively coupled discharge in a parallel plate configuration using SiH₄ as source gas, as illustrated in Fig. 1(a). The power density p_d and the process pressure P were controlled from 7 to 35 mW cm⁻² and from 40 to 267 Pa, respectively. The deposition temperature T_d was set to 200 °C. The thickness of the layers was determined by SE. Optical properties including the bandgap E_g (Tauc-gap) and the refractive index were also determined by SE, under the assumption of the Tauc-Lorentz model. In this study, refractive index at 1 eV ($n_{1\text{ev}}$) was characterized as a measure of the film density. The Si-H bond microstructure in these samples was analyzed by FT-IR. The signal-to-noise ratio in FT-IR spectra of such thin a-Si:H layers was improved by depositing the same films on both sides of the wafer. These layers are used as i_1 -layers for surface passivation on the p-side.

For characterizing surface passivation properties at the a-Si:H/c-Si interface with intrinsic bilayers ($i_1 + i_2$), we prepared n-type FZ-Si wafers (P-doped, $\sim 2\Omega\text{cm}$, $\langle 100 \rangle$ -oriented, 280-μm-thick) as substrates. These wafers were subjected to wet-chemical etching with a KOH-based solution to form random pyramidal textures on both surfaces. In

this process, wafers were etched by 5–10 μm in thickness on each surface. The average texture size was approximately 5 μm. Next, the textured wafers were subjected to wet-chemical cleaning with our standard cleaning process using H₂SO₄, H₂O₂, HCl, and HF.³¹ Then, intrinsic and doped a-Si:H layers were grown on both sides of the wafers by means of PECVD, using B₂H₆ and PH₃ as well as SiH₄ and H₂, as illustrated in Fig. 1(b). On the p-side, a series of i_1 -layers were applied with a fixed i_2 -layer grown with a hydrogen diluted plasma (SiH₄:H₂ = 1:10) at $P = 133\text{ Pa}$, $p_d = 7\text{ m Wcm}^{-2}$, and $T_d = 200\text{ }^\circ\text{C}$. In contrast, the i-layer on the n-side was fixed throughout this paper, although it was also grown using 2-step PECVD at $T_d = 200\text{ }^\circ\text{C}$. Therefore, we express the i-layer on the n-side as a single i-layer for simplicity, as illustrated in Fig. 1(b). The doped layers were grown at $P = 67\text{ Pa}$ and $p_d = 21\text{ m Wcm}^{-2}$ with a hydrogen diluted plasma (SiH₄:H₂ = 1:10) and a dopant gas (B₂H₆ or PH₃) concentration of approximately 0.2%. T_d of the p- and n-layers were set to 150 °C and 200 °C, respectively. The passivated wafers prepared had $i_2/i_1/\text{N}/i/\text{n}$ and $\text{p}/i_2/i_1/\text{N}/i/\text{n}$ structures, where N denotes an n-type c-Si wafer. The nominal thicknesses of a-Si:H layers on textured wafers were determined by using co-deposited films on flat wafers with SE for simplicity. Therefore, the actual thickness of each layer on textured wafers is expected to be thinner than the nominal value. The nominal thicknesses of the i-, p-, and n-layers were 10, 5, and 15 nm, respectively, while those of i_1 - and i_2 -layers were modified as shown in the following part. The effective minority carrier lifetime (τ_{eff}) of the passivated samples was characterized by quasi-steady state photoconductance (QSSPC) technique (Sinton Instruments, WCT-120), for quantifying the implied open circuit voltage (iV_{OC}) and the implied fill factor (iFF).

For completing SHJ solar cells, In₂O₃:Sn (ITO) films and Ag electrodes were formed with magnetron sputtering on both sides of the passivated wafer, followed by thermal annealing at 160 °C for 2 h, as illustrated in Fig. 1(c). Note that our front metal grid was not optimized, resulting in a relatively large shadow loss and series resistance. The current density-voltage (J-V) characteristics of the fabricated cells were evaluated using a solar simulator under air mass (AM) 1.5 and 100 mW cm⁻² illumination at 25 °C, and the open circuit voltage (V_{OC}), the short-circuit current density (J_{SC}), the fill factor (FF), and the conversion efficiency were recorded. All the cells were characterized under illumination

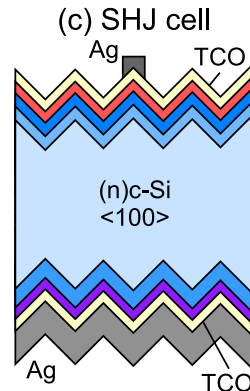
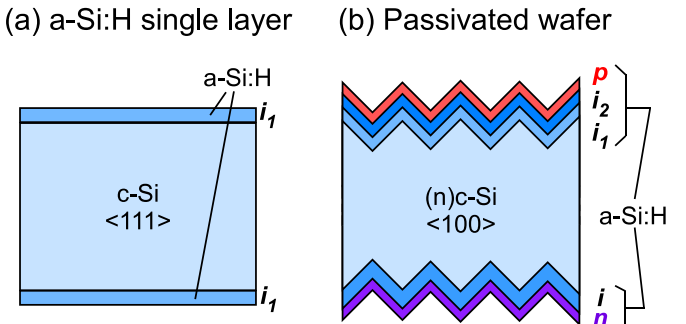


FIG. 1. Schematic illustrations of the samples prepared in this study: (a) a-Si:H single layers on polished high-resistivity FZ-Si wafer, (b) textured Si wafer passivated with a-Si:H stacks, and (c) SHJ solar cell.

from the p-layer side (front emitter). The cell area was 1.045 cm^2 designated by a shadow mask. Light-intensity dependent V_{OC} measurement (suns- V_{OC}) was also performed to extract the pseudo fill factor (pFF).³⁶ External quantum efficiency (EQE) spectra were measured with a Bunkou-Keiki, CEP-25BXS setup.

III. INTRINSIC a-Si:H LAYERS

A. Spectroscopic ellipsometry analysis

Figure 2 shows (a) the deposition rate (DR), (b) optical bandgap (E_g), and (c) refractive index at 1 eV (n_{1eV}) of very thin ($\sim 10\text{ nm}$) a-Si:H layers, as functions of p_d and P. These films were grown with pure SiH_4 plasma for the use as i_1 -layers, except the star symbols as described later. As shown in Fig. 2(a), the DR increases monotonically from 0.1 to 0.5 nm s^{-1} with an increase in p_d . This indicates that the film growth is simply enhanced by promoting the decomposition of SiH_4 molecules and increasing the precursor flux to the substrate surface. Conversely, the DR decreases to some extent with an increase in P, indicating that the precursor flux to the growth surface is reduced under such high P. This result is partly ascribed to the enhanced formation of Si nanoclusters in gas phase, which are preferentially exhausted out from the discharge region owing to their large mass.³⁷ Similar to the DR, the E_g of thin a-Si:H films increases monotonically from 1.65 to 1.85 eV with an increase in p_d , as shown in Fig. 2(b), which is ascribed to the increased

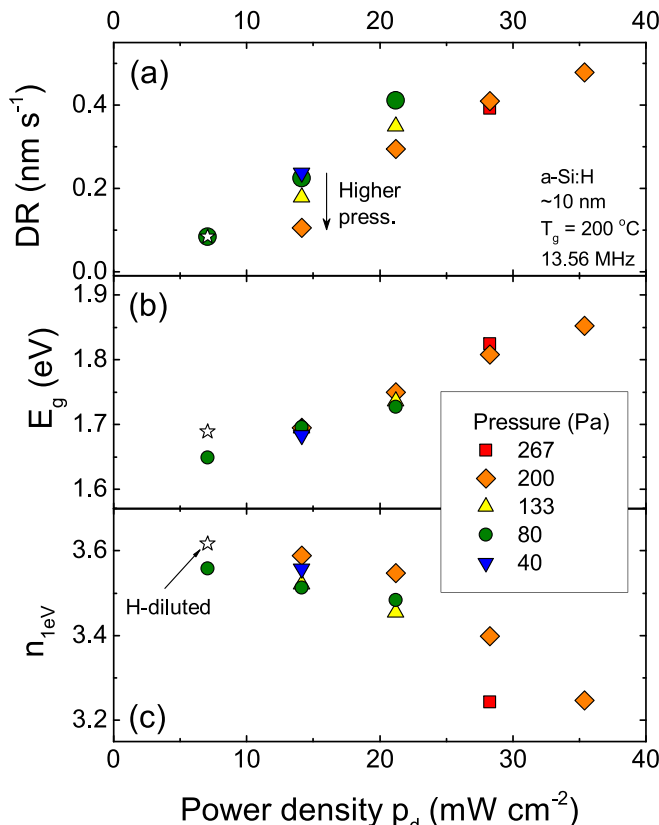


FIG. 2. (a) Deposition rate, (b) optical bandgap (E_g , Tauc gap), and (c) refractive index at 1 eV (n_{1eV}) of thin a-Si:H films ($\sim 10\text{ nm}$) as functions of the power density and the pressure in PECVD process. All the plots are the samples grown with pure SiH_4 plasma, except the star ($\text{SiH}_4:\text{H}_2 = 1:10$).

hydrogen content within the films, as discussed later. In contrast, the n_{1eV} of thin a-Si:H films shows a decreasing trend from 3.6 to 3.2 with an increase in p_d , particularly in case of $p_d > 27\text{ mW cm}^{-2}$, as shown in Fig. 2(c). The decrease in the n_{1eV} corresponds to the reduction in the film density. In general, such low-density a-Si:H films are defective and not suited to thin-film silicon solar cells, where a-Si:H itself acts as a photo-absorber material.³ In these graphs, we included the data of a-Si:H film grown with hydrogen-diluted plasma ($\text{SiH}_4:\text{H}_2 = 1:10$), which are shown by the star symbols and will be used as i_2 -layer in Secs. IV–VII. As shown in Fig. 2(c), this film shows the highest n_{1eV} among the samples, indicating that a denser film can be obtained by using hydrogen dilution.

B. FT-IR analysis

FT-IR is a powerful tool to investigate the microstructure of a-Si:H material. PECVD-grown a-Si:H films contain a significant amount of hydrogen, and most of them form Si-H bonds. Such Si-bonded hydrogen can be incorporated in the amorphous network in different manners, e.g., as an isolated Si-H and in the form of hydrogen clusters. In the latter case, $\text{Si}-\text{H}_2$ and $\text{Si}-\text{H}_3$ are grouped together preferentially at the surface of nano-sized voids.³⁸ The infrared absorption by the Si-H stretching vibration occurs at 2000 cm^{-1} for the isolated Si-H bonds (low-stretching mode, often termed “monohydride”), and at approximately 2100 cm^{-1} for the Si-H bonds associated with hydrogen clusters (high-stretching mode, often termed “dihydride”).^{39–42} Figure 3 shows the absorption coefficient spectra of thin a-Si:H films ($\sim 10\text{ nm}$) grown at different P and p_d , obtained by FT-IR. It is clearly seen that the absorption by high-stretching modes increases markedly with an increase in P and p_d , whereas that by low-stretching mode decreases slightly. This means that a-Si:H contains more hydrogen and becomes more void-rich at such conditions.⁴² In addition, a peak shift is observed for the absorption of high-stretching modes: the peak wavenumber shifts from 2090 to 2075 cm^{-1} with an increase in the peak intensity and then turns to shift oppositely to 2090 cm^{-1} with a further increase in the intensity. Similar observations were reported by Smets *et al.*⁴² It is worth to note that, even at very low P and p_d , the absorption peak of high-stretching modes in these films is rather high compared to that of thicker films.^{43,44} This result indicates that Si-H bonds corresponding to high-stretching modes are dominant in very thin a-Si:H films.⁴⁵

The absorption peak intensities of the low- and high-stretching modes, I_{LSM} and I_{HSM} , are quantified by curve fitting using Gaussian functions, as illustrated by the dotted curves in Fig. 3. The microstructure factor, R^* , is calculated by⁴⁶

$$R^* = I_{HSM}/(I_{LSM} + I_{HSM}). \quad (1)$$

In this definition, the higher R^* means the larger density of nano-sized voids in a-Si:H films. Figure 4 shows the R^* of thin a-Si:H films obtained in this study. The R^* increases from 0.3 to 0.9 by increasing p_d and P in PECVD process. However, the impact of P becomes less significant with an

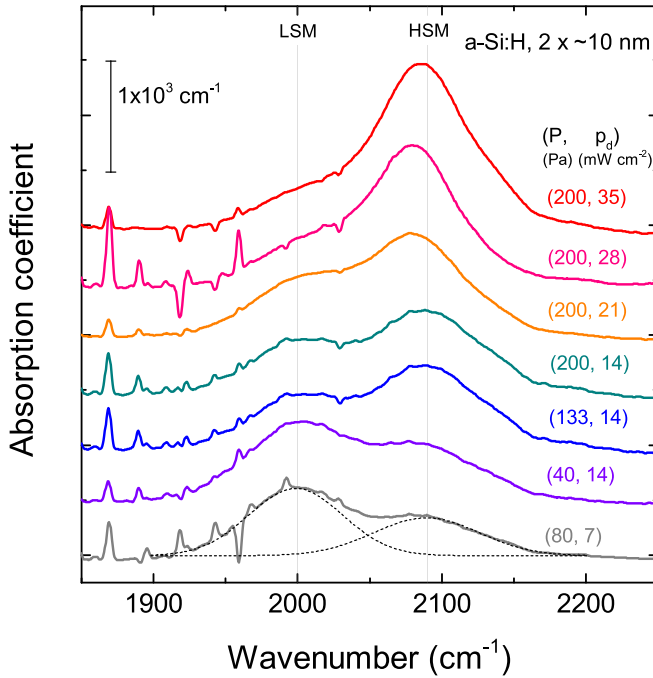


FIG. 3. Absorption coefficient spectra of thin a-Si:H films (~ 10 nm) grown at different pressures and power densities. Pairs of two numbers in brackets indicate the pressure P (Pa) and the power density p_d (mW cm^{-2}) used in PECVD process. The dotted lines show the fitting results with double Gaussian functions for the film grown at $P = 80$ Pa and $p_d = 7 \text{ mW cm}^{-2}$, for deconvolution of the absorption by Si-H bonds with the high- and low-stretching modes.

increase in p_d . It is also found that hydrogen dilution largely decreases R^* , as shown as the star symbol in Fig. 4.

Assuming that the fraction of free hydrogen without forming Si-H bonds is negligible, the hydrogen content C_H in a-Si:H films was estimated by⁴¹

$$C_H = \frac{P_C}{D} \int \frac{\alpha(\omega)}{\omega} d\omega \times 100 \text{ at. \%}, \quad (2)$$

where P_C denotes a proportionality constant of the Si-H bonding modes, D is the atomic density of a-Si:H films

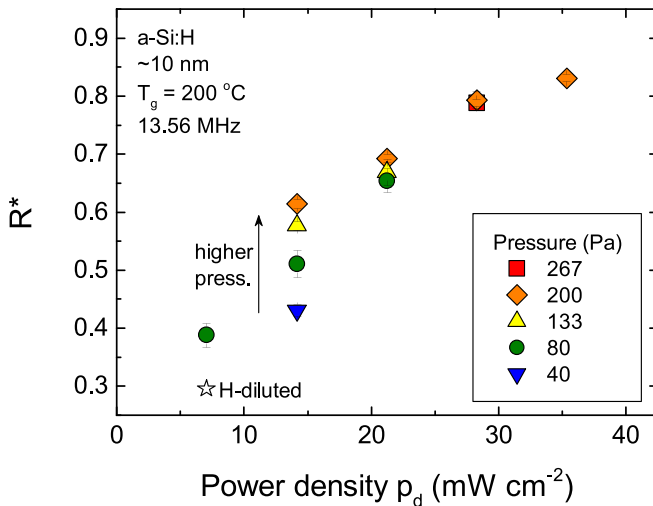


FIG. 4. Microstructure factor R^* of thin (~ 10 nm) a-Si:H films as functions of the power density and pressure in PECVD process. All the plots are the samples grown with pure SiH_4 plasma, except the star ($\text{SiH}_4:\text{H}_2 = 1:10$).

($5.0 \times 10^{22} \text{ cm}^{-3}$), α is the absorption coefficient for high- and low-stretching modes, and ω is the wavenumber. Here, we used $P_C = 9.0 \times 10^{19}$ and $2.2 \times 10^{20} \text{ cm}^{-3}$ for the Si-H low- and high-stretching modes, respectively.⁴¹ Figure 5 shows the estimated C_H as a function of R^* . It is found that, with an increase in R^* , the C_H for the low-stretching mode ($C_{H-\text{LSM}}$) decreases gradually from 5% to 2%, whereas that for the high-stretching mode ($C_{H-\text{HSM}}$) increases steeply from 6% to 22%. Consequently, the total hydrogen content ($C_{H-\text{total}}$) is governed by the $C_{H-\text{HSM}}$ and shows a monotonic increase from 11% to 25% with an increase in R^* . It is known that the E_g of a-Si:H has a positive correlation with the hydrogen content within the film.³⁸ This is also valid in our case, as can be confirmed by the comparison of Figs. 2(b) and 5. Therefore, the increase in the E_g in Fig. 2(b) is ascribed to the increased hydrogen content within the films.

IV. SURFACE PASSIVATION

A. Effect of the intrinsic bilayer

In this section, we focus on the impact of intrinsic bilayers on surface passivation at the a-Si:H/c-Si interface. Figure 6 shows the τ_{eff} of passivated wafers with i/N/i/n and p/i/N/i/n structures as a function of the excess carrier density Δn . In this graph, only the i-layer on the p-side is modified in the following manner: (i) single i_1 -layer (10 nm), (ii) single i_2 -layer (10 nm), and (iii) a stack of i_1 - and i_2 -layers (4 + 6 nm). The i_1 -layer was grown under the conditions of $P = 200$ Pa and $p_d = 28 \text{ mW cm}^{-2}$ using pure SiH_4 plasma, whereas the i_2 -layer was grown under the fixed conditions described in Sec. II. Note that the condition of the i_2 -layer enables us to obtain “good” a-Si:H films as semiconductor material. The single i_2 -layer realizes relatively good surface passivation in the i/N/i/n structure, resulting in a τ_{eff} of approximately 3 ms at $\Delta n = 1 \times 10^{15} \text{ cm}^{-3}$. However, after the p-layer deposition, the τ_{eff} decreases largely over the entire range of Δn . This means that the interface recombination is enhanced by the deposition of the overlying p-layer, which is ascribed to the increased density of the interfacial

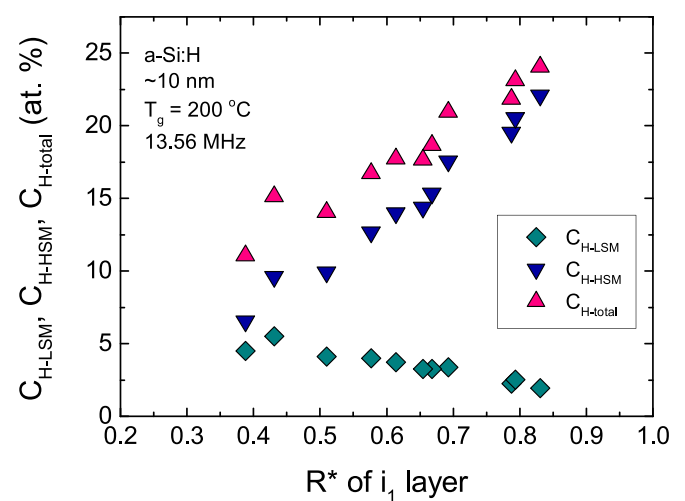


FIG. 5. Hydrogen content in very thin (~ 10 nm) a-Si:H films grown with pure SiH_4 plasmas calculated using FT-IR spectra as a function of R^* .

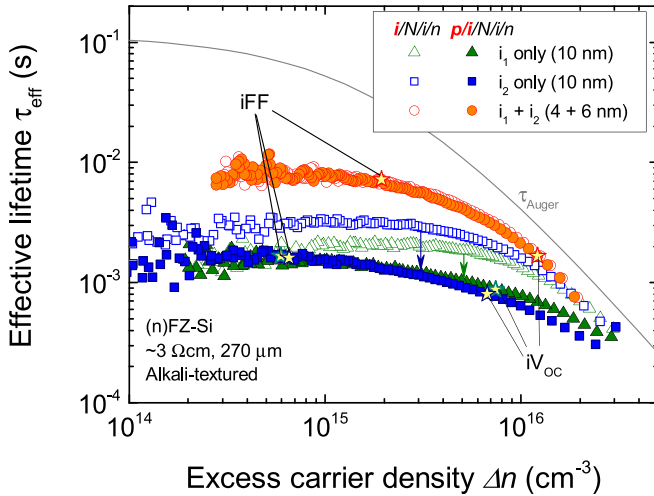


FIG. 6. Effective lifetime τ_{eff} of passivated wafers with $i/N/i/n$ and $p/i/N/i/n$ structures as a function of excess carrier density Δn . Three different i -layers were applied on the p-side: a single $i_1/N/i/n$ and $p/i_1/N/i/n$, a single $i_2/N/i/n$ and $p/i_2/N/i/n$, and a stack of i_1 - and i_2 -layers ($i_2/i_1/N/i/n$ and $p/i_2/i_1/N/i/n$). The growth conditions of the i_1 - and i_2 -layers are described in the text. The star symbols indicate the τ_{eff} corresponding to iV_{OC} and iFF in the $p/i/N/i/n$ samples.

defects, probably related to partial crystallization of the a-Si:H layer at the a-Si:H/c-Si interface. In contrast, τ_{eff} is improved significantly by inserting the thin i_1 -layer between the i_2 -layer and the c-Si surface. Moreover, the τ_{eff} is maintained at a similar level even after the p-layer deposition. Interestingly, the single i_1 -layer results in the lowest τ_{eff} regardless of the existence of the p-layer, as shown in Fig. 6. This indicates that the passivation property of the i_1 -layer itself is rather poor, and an additional “good” a-Si:H layer is necessary for improving the passivation. These results clearly demonstrate the benefit of using intrinsic bilayers for improving surface passivation at the a-Si:H/c-Si interface, especially after the p-layer deposition.

Next, we investigate the effect of the thickness of the i_1 -layer in intrinsic bilayers. Figure 7 shows (a) the τ_{eff} at $\Delta n = 1 \times 10^{15} \text{ cm}^{-3}$, (b) the iV_{OC} , and (c) the iFF of passivated wafers with $i/N/i/n$ and $p/i/N/i/n$ structures, as functions of the i_1 -layer thickness. Here, the total thickness of the intrinsic bilayers ($i_1 + i_2$) on the p-side is fixed at 10 nm, and the i_1 -layer thickness is varied from 0 to 10 nm. The growth conditions of the i_1 - and i_2 -layers are the same as those used in Fig. 6. Each plot in Fig. 7 indicates the data taken from one passivated wafer. It is clearly seen in Fig. 7(a) that the τ_{eff} of the $i_2/i_1/N/i/n$ samples is drastically improved by the insertion of a very thin (~2 nm) i_1 -layer. It takes the maximum value of ~10 ms at the i_1 -layer thickness of 2–4 nm and then turns to decrease as the thickness is increased further. The τ_{eff} after the p-layer deposition shows a similar trend, as shown in Fig. 7(a). However, in this case, the τ_{eff} depends on the i_1 -layer thickness more significantly than before the p-layer deposition. As a result, the maximum value of ~8 ms is obtained at the i_1 -layer thickness of ~4 nm. Similarly, the iV_{OC} is largely improved by using bilayers, particularly in the $p/i/N/i/n$ samples, as shown in Fig. 7(b). However, the i_1 -layer thickness does not have a significant impact on the iV_{OC} , as long as the i -layer has the

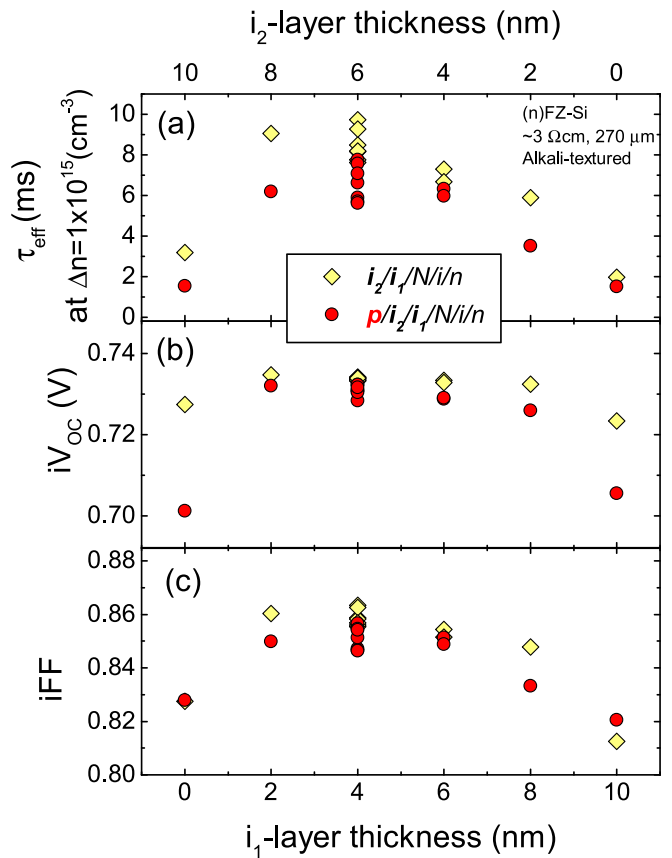


FIG. 7. Effect of the i_1 - to i_2 -layer thickness ratio on the effective lifetime, iV_{OC} , and iFF of passivated wafers with $i_2/i_1/N/i/n$ and $p/i_2/i_1/N/i/n$ structures. The total thickness of the intrinsic bilayers ($i_1 + i_2$) on the p-side is fixed at 10 nm.

bilayer structure; high iV_{OC} exceeding 0.73 V can be obtained in a wide range of the i_1 -layer thickness from 2 to 6 nm. The behavior of the iFF is very similar to that of the τ_{eff} as shown in Fig. 7(c), having a peak value of 0.86 at the i_1 -layer thickness of ~4 nm. It is also found from Figs. 7(b) and 7(c) that the peak of iV_{OC} is broader than that of iFF, revealing that iFF is more sensitive to recombination compared to iV_{OC} . A similar trend was also reported by Haschke *et al.* using numerical simulations.⁴⁷ From these results, we conclude that the optimum i_1 -layer thickness is ~4 nm in this series of experiment. However, this value might be dependent on the growth conditions and the total i -layer thickness.

B. Effect of the microstructure in the interfacial layer (i_1 -layer)

In this subsection, we investigate the effect of the microstructure in i_1 -layers, represented by R^* , on surface passivation. Here, the thicknesses of i_1 - and i_2 -layers on the p-side are fixed at 4 and 6 nm, respectively, based on the results shown in Fig. 7. Figure 8 shows (a) the iV_{OC} and (b) the iFF of the passivated wafers with the $i_2/i_1/N/i/n$ and $p/i_2/i_1/N/i/n$ structures, as a function of R^* of the i_1 -layers. It is confirmed in Fig. 8(a) that the iV_{OC} of the $i_2/i_1/N/i/n$ samples increases gradually with an increase in R^* and then saturates. Accordingly, a peak iV_{OC} of approximately 0.734 V is

obtained at an R^* of approximately 0.7. The impact of R^* on iV_{OC} becomes more pronounced in the case of the $p/i_2/i_1/N/i/n$ samples; the iV_{OC} reduction after the p-layer deposition is largely mitigated by increasing the R^* . Accordingly, the best iV_{OC} in the $p/i_2/i_1/N/i/n$ samples is obtained at an R^* of approximately 0.8, which is almost the highest R^* we obtained in this study. We find a similar trend also in the iFF, as shown in Fig. 8(b). Thus, the degradation of surface passivation induced by overlying p-layers is mitigated by applying an i_1 -layer with large R^* , resulting in high iV_{OC} and iFF. In this study, the i_1 -layers with high R^* were obtained under high-P and high- p_d conditions in the PECVD process. As already shown in Figs. 2 and 5, i_1 -layers grown under these conditions have more porous structures and contain a large quantity of hydrogen. It is expected that the insertion of such films at the a-Si:H/c-Si interface is efficient in preventing partial crystallization of the a-Si:H layer at the a-Si:H/c-Si interface during the p-layer deposition, as reported by Liu *et al.*²² However, such porous a-Si:H films themselves are less efficient for surface passivation, as already shown in Fig. 7 (see the data at the i_1 -layer thickness of 10 nm), which is ascribed to the large density of defects. Therefore, an additional i_2 -layer with a denser microstructure is required to obtain high iV_{OC} and iFF. In case of the single i_2 -layer without i_1 -layer, iV_{OC} and iFF are already rather poor even before p-layer deposition, suggesting that the

partial epitaxial growth at the a-Si:H/c-Si interface already occurs during i_2 -layer deposition.

V. SOLAR CELLS

A. Photovoltaic parameters

In this section, we move our focus to the impact of the i_1 -layers on the photovoltaic performance of SHJ solar cells. The cell precursors, i.e., passivated wafers with the $p/i_2/i_1/N/i/n$ structure, are equivalent to those used in Sec. III B. Figure 9 summarizes the J-V parameters of the SHJ solar cells fabricated in this study as a function of R^* of the i_1 -layer, which is the main result in this study. All the data shown in Fig. 9 are averaged values, as more than 8 cells with an area of 1.045 cm^2 were processed for each condition. The error bars indicate the standard deviation. As shown in Fig. 9(a), the V_{OC} in the SHJ solar cells increases almost monotonically with an increase in R^* of the i_1 -layer. This trend is consistent with the results of the iV_{OC} shown in Fig. 7(a), although the absolute values of the V_{OC} are smaller than the iV_{OC} , probably due to the process-induced damage during the metallization process (sputtering)⁴⁸ and the perimeter effect.⁴⁹ The latter seems to give a significant effect in our case because the area of our SHJ solar cells is rather small. Similar to the V_{OC} , the pFF in the SHJ solar cells increases almost monotonically with an increase in R^* , as expected from Fig. 8(b). These results for the V_{OC} and the pFF clearly demonstrate that the application of an interfacial layer (i_1 -layer) with a high R^* is advantageous to improve the surface passivation in SHJ solar cells.

The difference between the pFF and the FF, ΔFF , is attributed to the series resistance. The origins of the series resistance can be categorized into two components, i.e.: (i) losses related to the grid design (sheet resistivity loss in the ITO layer and the line resistivity loss in the Ag grid), and (ii) losses related to the carrier transport from c-Si to the ITO layer (at the a-Si:H/c-Si and a-Si:H/ITO interfaces and within a-Si:H layers). The ΔFF observed here is rather large compared to the results from other groups,⁹ mainly due to the losses related to the non-optimized Ag grid as mentioned before. If the series resistance is governed only by these losses, then the ΔFF in this graph is supposed to be constant. However, we find that several samples show larger ΔFF compared to the others, as marked with a dashed circle in Fig. 9(b). For example, in the case of the cells with the i_1 -layers grown at 200 Pa, the FF increases with an increase in R^* but turns to decrease steeply after peaking at $R^* \sim 0.8$, in spite of the high pFF. Moreover, the relatively high ΔFF are observed in a wide range of the growth pressure. These results suggest that the carrier transport property within the intrinsic bilayers and/or the a-Si:H/c-Si interface is strongly affected by the growth condition of the i_1 -layer, even if its thickness is less than a half of the total thickness of the bilayers. This is one of the important findings in this study.

In contrast to V_{OC} and pFF, J_{SC} shows a monotonic decrease with an increase in R^* as shown in Fig. 9(c). This result clarifies another drawback accompanied by the incorporation of i_1 -layers with high R^* . The reason for the J_{SC} decrease will be discussed later, though it is not completely

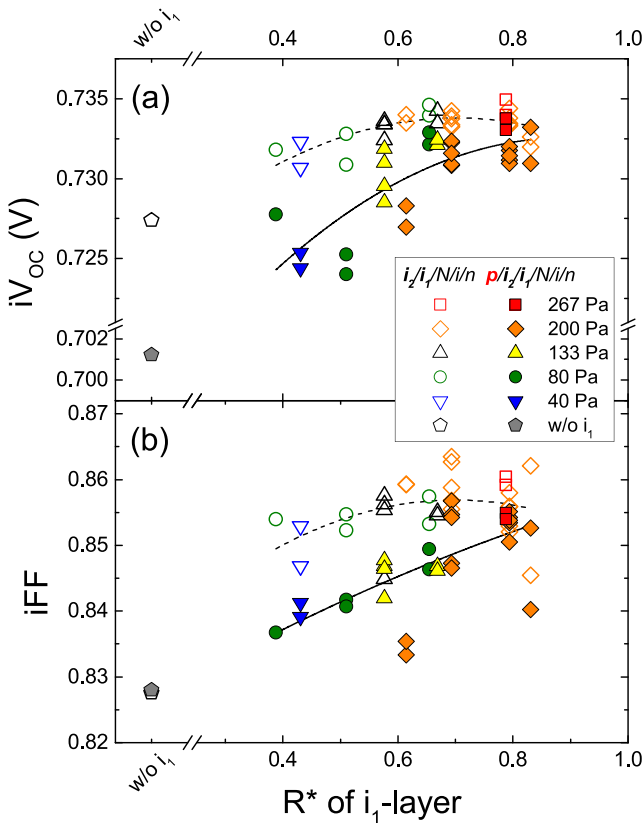


FIG. 8. (a) iV_{OC} and (b) iFF of the passivated wafers with $i_2/i_1/N/i/n$ and $p/i_2/i_1/N/i/n$ structures, as a function of the microstructure factor R^* of the i_1 -layers on the p-side. The difference in symbol shapes corresponds to the difference in the growth pressure P of i_1 -layers as shown in the legend. The dashed and solid lines are guides to the eye for the $i_2/i_1/N/i/n$ and $p/i_2/i_1/N/i/n$ structures, respectively.

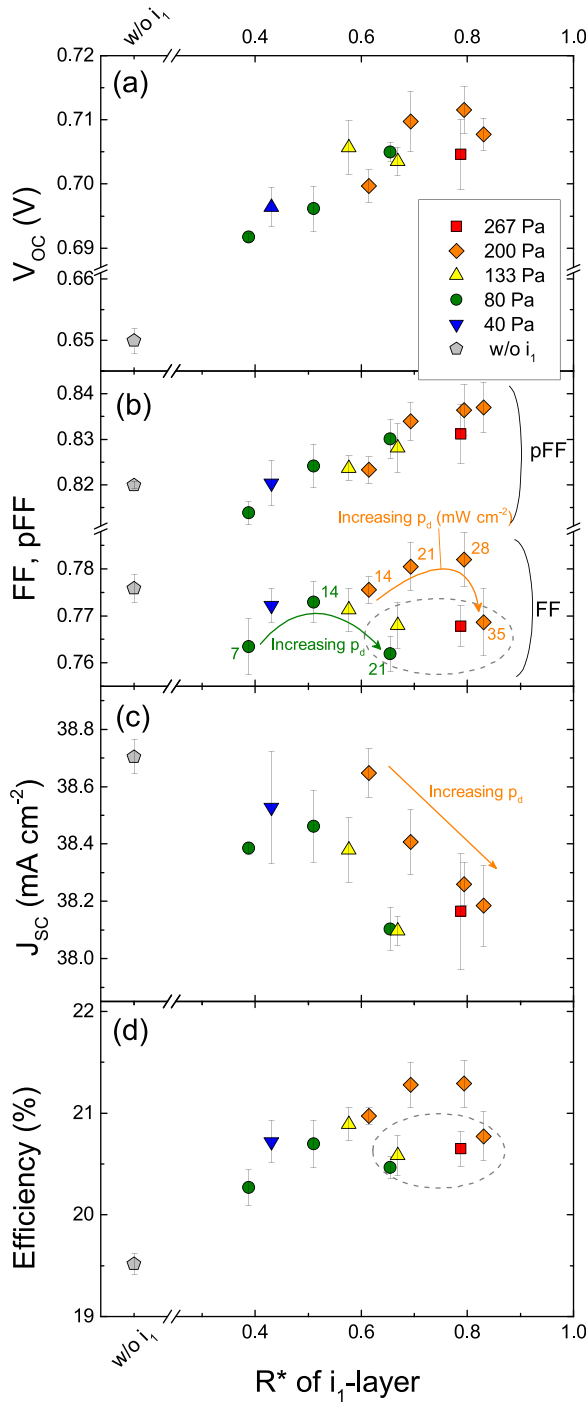


FIG. 9. J-V parameters of SHJ solar cells fabricated in this study as a function of R^* of the i_1 -layer: (a) V_{OC} , (b) pFF and FF, (c) J_{SC} , and (d) conversion efficiency. All the plotted data are averaged value of more than 8 cells for each condition and the error bars indicate the standard deviation. The difference in symbol shapes corresponds to the difference in the growth pressure P of i_1 -layers as shown in the legend. The numbers close to the FF plots in (b) indicate the corresponding power densities p_d (mW cm^{-2}) for the growth of i_1 -layers.

clear yet. However, the J_{SC} loss ($<2\%$) is smaller than the gain in V_{OC} ($>2\%$) and FF ($>2\%$). Accordingly, the conversion efficiency of SHJ cells increases from 19.5% to 21.3% on average, by using intrinsic bilayers. The best cell in this series of experiment showed a conversion efficiency of 21.9% ($J_{SC}=38.4 \text{ mA cm}^{-2}$, $V_{OC}=0.717 \text{ V}$, FF = 0.795, and pFF = 0.841).

B. Quantum efficiency

Here, we use EQE spectra to examine the origin of the J_{SC} reduction caused by the use of a bilayer structure. Figure 10(a) shows typical EQE spectra of the SHJ cells using intrinsic bilayers on the p-side interface. In this figure, all the cells have the same structure except for the growth conditions of the i_1 -layer. It is clearly observed that the EQE in the short wavelength region ($<600 \text{ nm}$) decreases with an increase in R^* of the i_1 -layer, which causes the reduction in J_{SC} from 38.7 (without i_1 -layer) to 38.0 mA cm^{-2} ($R^*=0.83$). To emphasize the spectral variation in these samples, we calculated the difference in EQE, ΔEQE , which is defined as $\Delta\text{EQE}=\text{EQE}(\text{with } i_1\text{-layer})-\text{EQE}(\text{without } i_1\text{-layer})$. It is clearly shown in Fig. 10(b) that the reduction in J_{SC} mostly originates from the ΔEQE in the range of 400–550 nm. In general, current loss due to the a-Si:H p/i stack at the front side is caused by several reasons: (i) variation in its actual thickness, (ii) variation in its absorption coefficient, and (iii) variation in the collection probability of photo-generated carriers within the p/i stack. The reason (i) could occur because of the epitaxial growth during the cell process, even though we monitored the film thickness by using the co-deposited film on a flat wafer. However, it is difficult to explain the wavelength dependence of the ΔEQE only by the thickness difference, and therefore this effect should be minor.³⁵ The reason (ii) is not likely, because the variation of the absorption coefficient in the p/i stack is not sufficient to cause the variation in the ΔEQE , according to our SE results. Therefore, the main origin of the ΔEQE could be accounted for by reason (iii) in this case. It is known that a portion of the photo-generated minority carriers (electron in this case) within the i-layer can be transferred to the c-Si wafer and contribute to the photocurrent.^{35,50} The collection

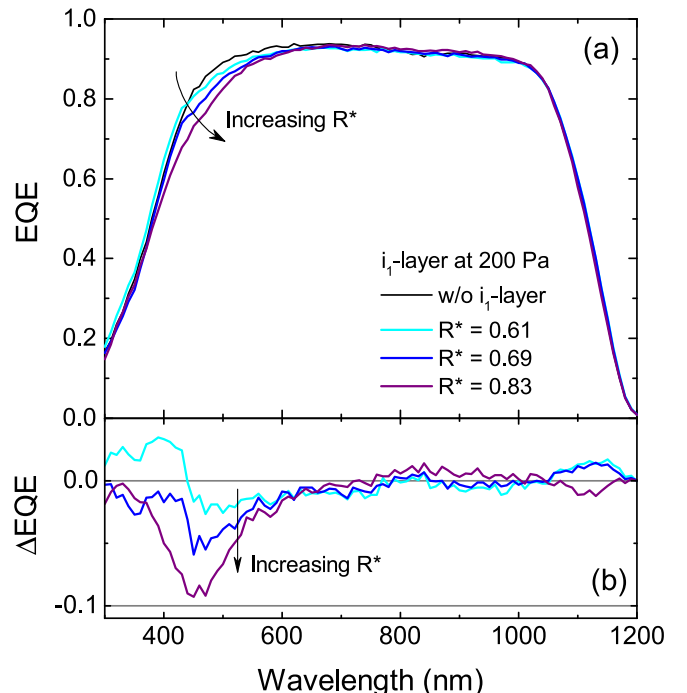


FIG. 10. EQE spectra of the SHJ cells with different i_1 -layers: (a) Raw EQE spectra and (b) difference EQE (ΔEQE).

of such carriers is presumably impeded by using i_1 -layers with high R^* , because such layers are more disordered. This effect could be wavelength-dependent, since carrier collection is expected to be more efficient when the location of photo-carrier generation becomes closer to the c-Si surface. This topic will be shortly discussed later.

C. TEM observation

The microstructure at the a-Si:H/c-Si interface of selected SHJ solar cells was investigated by transmission electron microscopy (TEM). Here, we chose two SHJ cells from Fig. 9, i.e., the best-performing cell using an intrinsic bilayer with the stack of the i_1 - ($p_d = 28 \text{ mW cm}^{-2}$ and $P = 200 \text{ Pa}$) and i_2 -layers and the cell using the single i_2 -layer (without i_1 -layer), as an extreme comparison. The TEM observation was performed on the {111} facet of a pyramidal texture on the p-side surface. Figure 11 shows the cross-sectional TEM images of the a-Si:H/c-Si interfaces of the two SHJ cells. It is clarified that an abrupt a-Si:H/c-Si interface was obtained by using the bilayer, as shown in Fig. 11(a). In contrast, in the latter case, partial crystallization was clearly observed at the a-Si:H/c-Si interface, as shown in Fig. 11(b). This leads to the reduction of the effective thickness of the a-Si:H passivating layer, resulting in the deteriorated surface passivation. Moreover, in Fig. 11(b), the dark region was observed within the c-Si wafer directly beneath the a-Si:H/c-Si interface, indicating that this region contains strain and/or lattice defects. This could be ascribed to the strain which is induced by partial crystallization of a-Si:H at the interface and/or process-induced damage during PECVD with hydrogen-rich plasma for the growth of the i_2 -layer, although more detailed analysis has to be done to clarify this point. This suggests that the insertion of i_1 -layers is beneficial to prevent partial crystallization and to reduce the strain at the interface.

Here, we compare the actual a-Si:H thickness on textured wafers with the nominal thickness which was determined by using co-deposited films on flat wafers. From Fig. 11, the total thickness of the i/p a-Si:H stack was determined to be approximately 10 nm, whereas the nominal thickness was 15 nm ($i + p = 10 + 5 \text{ nm}$) in these cells. Therefore, the ratio of the thickness on the pyramidal textures to that on planer wafers is approximately 2/3 (0.67), which is in good agreement with the previous report (0.69).⁵¹

D. SHJ cell with thin wafer

It is well known that the V_{OC} of c-Si solar cells is strongly dependent on the wafer thickness.^{6,11,13,52} In Secs. VA–VC, we used the relatively thick ($\sim 270 \mu\text{m}$) FZ-Si wafers as a standard material, resulting in the best V_{OC} of approximately 0.720 V. This is because we aimed to avoid any unintentional variation in the quality of substrates. Here, we show the result of a SHJ cell using a thinner wafer. The cell fabrication process was the same as we used in Secs. VA–VC, except the wafer. Figure 12 shows the current-voltage curve of a SHJ cell with a P-doped n-type Czochralski (CZ)-grown monocrystalline Si wafer ($\sim 2 \Omega \text{ cm}$,

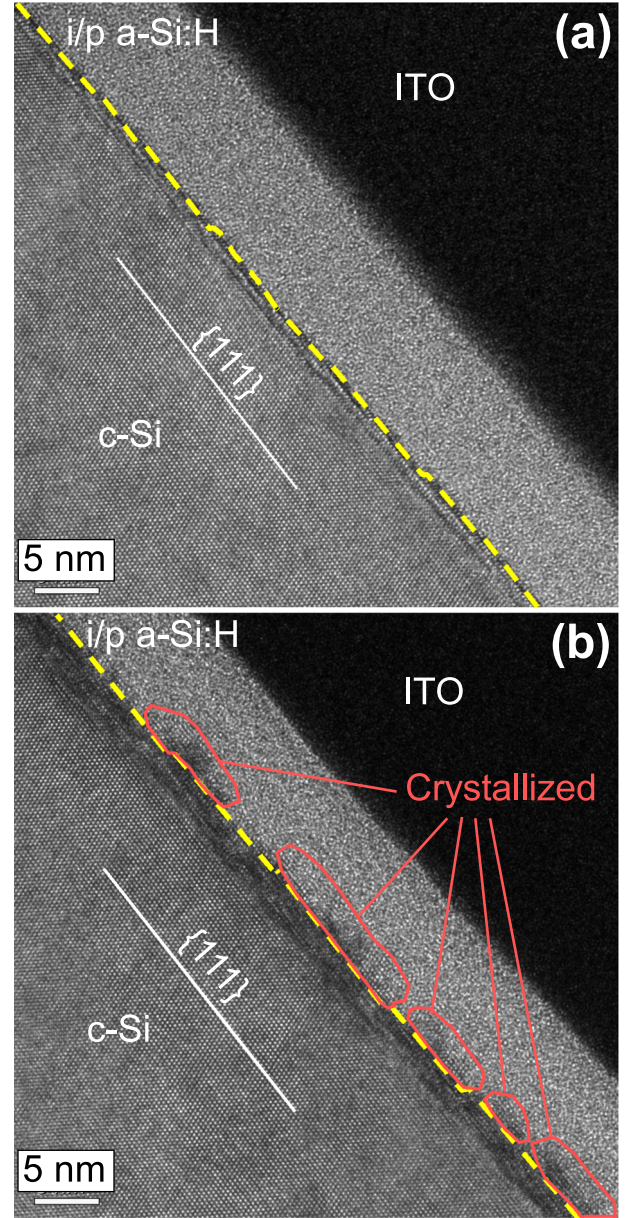


FIG. 11. Cross-sectional TEM images near the p-side a-Si:H/c-Si interfaces of the SHJ solar cells with (a) the intrinsic bilayer ($i_1 + i_2$) and (b) the single-layer (i_2). In the latter case, partial crystallization is observed near the interface. The yellow lines in the figures indicate the a-Si:H/c-Si interface.

$\langle 100 \rangle$ -oriented), with an average thickness of $85 \mu\text{m}$ after texturing. As shown in Fig. 12, a high V_{OC} of 0.742 V was confirmed in the cell, despite suffering from the perimeter recombination due to the small cell size (1.045 cm^2).⁴⁹ Accordingly, a high conversion efficiency of 22.2% was obtained, although the J_{SC} and the FF were largely limited by the front electrode design, as mentioned earlier.

VI. DISCUSSION

A. Impact of the i_1 -layer on surface passivation

The R^* of the i_1 -layer in the intrinsic bilayer is closely correlated to the surface passivation properties at the a-Si:H/c-Si interface, particularly after the deposition of overlying p-layers, as confirmed in Fig. 8. According to the results

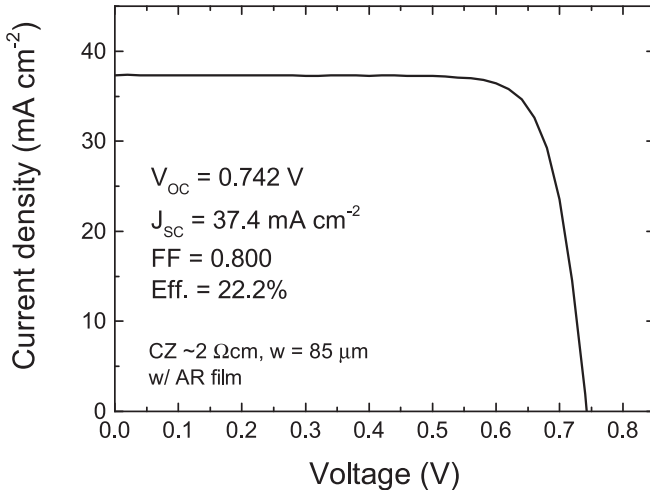


FIG. 12. Current density-voltage curve of a thin SHJ cell with a wafer thickness of 85 μm . The optimized intrinsic bilayer was applied to the p-side passivation. The cell area is designated at 1.045 cm^2 with a shadow mask. An anti-reflection (AR) film with moth-eye structure⁵³ was applied.

shown in Figs. 2(c), 4, and 5, a-Si:H films become more porous with an increase in R^* , which is more effective in preventing partial crystal formation at the a-Si:H/c-Si interface. Thus, improved surface passivation at the a-Si:H/c-Si interface by using i_1 -layers with high R^* is ascribable to the suppression of the partial crystallization, which is also partly confirmed through TEM observations, as shown in Fig. 11. However, the conversion efficiency of SHJ solar cells is not necessarily improved by simply increasing the R^* of the i_1 -layer, as shown in Fig. 9. High R^* is necessary for good surface passivation, but not sufficient to realize a high efficiency, because it also causes an increase in the series resistance and the J_{SC} loss for some cases.

B. Impact of the i_1 -layer on series resistance

In the case of our SHJ cells, photo-generated holes have to pass through the intrinsic bilayers as majority carriers to be collected at the electrode. Therefore, ΔFF can be regarded as a measure of the resistance in a-Si:H bilayers for majority carrier transport. If the interfacial a-Si:H layer behaves as a very poor transport channel, then the ΔFF of the SHJ cell will increase significantly. It is expected that a-Si:H films become less efficient in carrier transport due to an increase in their porosity or degree of disorder. Figure 13 shows the correlation between the ΔFF and the R^* of the i_1 -layers, which is a re-plot of the results shown in Fig. 9(b). It is clearly seen that the ΔFF tends to increase with an increase in R^* for i_1 -layer deposited at the same pressure. This reveals that carrier transport property in a-Si:H films is closely correlated to R^* . However, it is also found that the increase in ΔFF can be mitigated by increasing the growth pressure, even with similar R^* values. In other words, one can increase R^* of a-Si:H films, i.e., improve surface passivation at the a-Si:H/c-Si interface, without sacrificing ΔFF by increasing the growth pressure. This suggests a pathway to improve the conversion efficiency of SHJ cells further.

We also notice that the sample grown at 267 Pa, which is the highest P used in this study, shows a different

behavior. This could be ascribed to the rather porous a-Si:H network in this condition, as confirmed by the very low n_{lev} in Fig. 2(c). This indicates that the film porosity (density) is not necessarily linked with R^* . The behavior of the i_1 -layers at this pressure should be investigated in more detail. However, unfortunately, we could not obtain other data points at this pressure in this series of experiment because of the instability of the plasma discharge.

It is known that carrier transport can be also affected by the band offsets at the a-Si:H/c-Si interface, as often observed in SHJ cells with a-SiO_x:H passivating layers.⁵⁴ However, in our case, ΔFF is not simply linked to the band gap (Tauc gap) of i_1 -layers. Therefore, carrier transport is likely affected by the defects and traps within the a-Si:H channel, rather than the band offset. However, further studies are needed to clarify the origin of the deteriorated carrier transport.

C. Correlation between losses in FF and current density

Figure 14 shows the correlation between the ΔFF and the ΔJ_{SC} , which is defined as the reduction of the J_{SC} with respect to the cell without i_1 -layer. It is confirmed that the ΔJ_{SC} increases almost linearly with an increase in ΔFF in the range of $\Delta\text{FF} < 0.06$, revealing that these losses are closely correlated in this range. However, in the range of $\Delta\text{FF}^* > 0.06$, ΔJ_{SC} remains almost constant in spite of the further increase in ΔFF . Thus, the reduction of the J_{SC} caused by using i_1 -layers with high R^* seems to be saturated at a certain point. We tentatively ascribe this result to the variation of the collection probability of photo-generated carriers within the i -layer, β . According to Holman *et al.*,³⁵ the β of the i -layers in SHJ cells ranges from 0.2 to 0.5, i.e., 20%–50% of photo-generated carriers are transferred to the c-Si wafer and collected at the electrode. Recently, Paduthol *et al.* also characterized the β by photoluminescence measurement and

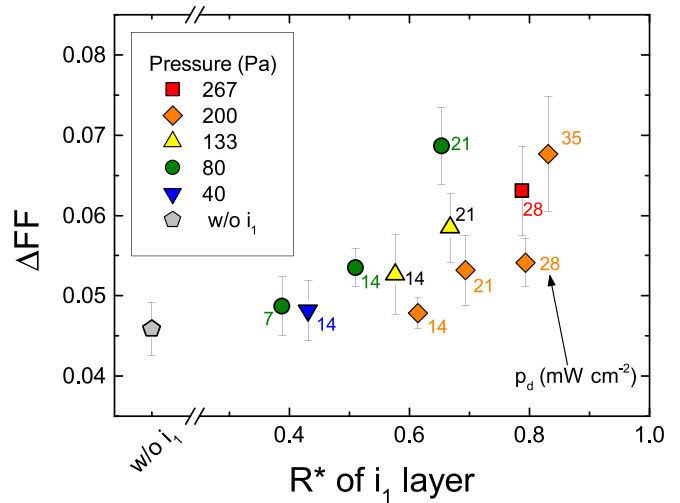


FIG. 13. ΔFF ($= p\text{FF} - \text{FF}$) of SHJ solar cells fabricated in this study as a function of R^* of the i_1 -layer. The difference in symbol shapes corresponds to the difference in the growth pressure P of i_1 -layers as shown in the legend. The numbers close to the plots indicate the corresponding power densities p_d (mW cm^{-2}) for the growth of i_1 -layers.

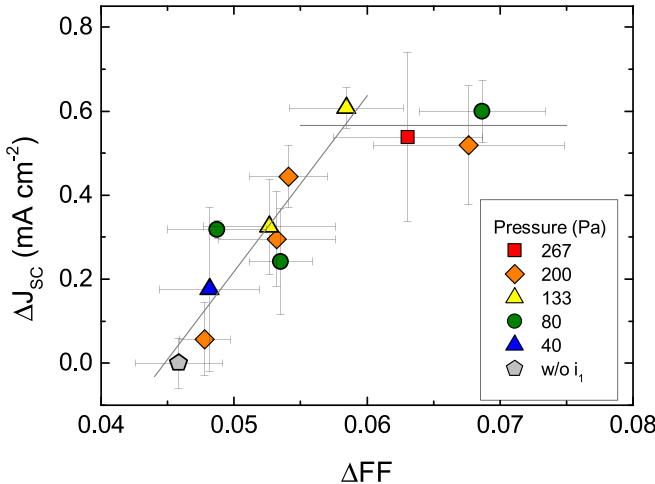


FIG. 14. Correlation between ΔV_{oc} and ΔJ_{sc} of SHJ solar cells fabricated in this study. The solid lines are guides to the eye.

reported that the β is approximately 0.4 when the i_1 -layer is capped with an p -layer.⁵⁵ The ΔJ_{sc} behavior can be explained if the β decreases with an increase in R^* of the i_1 -layer and then saturates, whether it means the i_1 -layer is a completely “dead” layer ($\beta \sim 0$) or not. The ΔEQE results shown in Fig. 10(b) suggest that β is wavelength-dependent. This point must be addressed in more detail in the future. In contrast, the ΔFF is not expected to be saturated in the range shown in Fig. 14, since the transport of majority carriers is expected to be impeded more by using more porous and disordered i_1 -layers.

D. Effect of thickness of the i_1 -layer

In this study, the thicknesses of i_1 - and i_2 -layers are fixed at 4 and 6 nm, respectively, which were derived from the best lifetime result shown in Fig. 7, using fixed PECVD conditions. The best thickness may become thinner than 4 nm with an increase in R^* , supposing that the main function of the i_1 -layer is to prevent the epitaxial growth at the a-Si:H/c-Si interface. In addition, the best thickness for the i_1 -layer can be dependent on the PECVD condition of the i_2 -layers and subsequently deposited (doped) layers. Furthermore, use of porous i_1 -layers gives an impact not only on surface passivation but also on the J_{sc} and the series resistance, as shown in Fig. 9. This means that the thickness combination for the best efficiency can be different from that for the best passivation. Thus, our best condition for the intrinsic bilayer obtained in this study has not been fully optimized yet, and there is room for improvement.

VII. CONCLUSIONS

In this study, we investigated the impact of intrinsic a-Si:H bilayers, which are composed of a porous interfacial layer and a dense layer, on the photovoltaic performance in SHJ solar cells. For the bilayer configuration, the microstructure factor R^* of the interfacial layer is a good measure for surface passivation; using an interfacial layer with high R^* leads to suppressed crystallization and better surface passivation at the a-Si:H/c-Si interface, resulting in improvements in the V_{oc} and the pFF. However, the conversion efficiency of SHJ solar cells is not necessarily improved by simply

increasing the R^* , because it also causes negative effects including the increase in the series resistance and the J_{sc} loss. The series resistance loss is linked to the majority carrier transport, whereas the J_{sc} loss observed in this study seems to be related to the minority carrier recombination loss within the a-Si:H p/i stack. Thus, the interfacial layer plays also an important role in both the majority and the minority carrier transport. In addition, it is found that the series resistance loss is mitigated by increasing the growth pressure, even with similar R^* values, suggesting a route for further improvements. These results indicate that R^* of the interfacial layer is important, but not the sole parameter for realizing high-efficiency SHJ cells. Since we varied only the power density and the pressure in this study, the effects of other growth parameters, including temperature, excitation frequency, and gas species, should be investigated in detail. Besides, one can expect that a more complex multi-step growth would lead to a better performance in SHJ solar cells.²⁷ Moreover, the precise control of i_1 -layers on the n-side is also important, though its impact is smaller than on the p-side.^{13,33}

ACKNOWLEDGMENTS

The authors thank T. Oku, Y. Sato, A. Sato, and M. Tanabe for the technical support in this work and T. Kawatsu of Komatsu NTC Ltd. for preparing thin Si wafers. A part of this work was conducted under a project commissioned by the New Energy and Industrial Technology Development Organization (NEDO), Japan.

- ¹M. Tanaka, M. Taguchi, T. Matsuyama, T. Sawada, S. Tsuda, S. Nakano, H. Hanafusa, and Y. Kumano, *Jpn. J. Appl. Phys., Part 1* **31**, 3518 (1992).
- ²S. De Wolf, A. Descoedres, Z. C. Holman, and C. Ballif, *Green* **2**, 7 (2012).
- ³M. Stuckelberger, R. Biron, N. Wyrtsch, F.-J. Haug, and C. Ballif, *Renewable Sustainable Energy Rev.* **76**, 1497 (2017).
- ⁴H. Sai, T. Matsui, and K. Matsubara, *Phys. Status Solidi A* **214**, 1700544 (2017).
- ⁵M. Taguchi, A. Yano, S. Tohoda, K. Matsuyama, Y. Nakamura, T. Nishiwaki, K. Fujita, and E. Maruyama, *IEEE J. Photovoltaics* **4**, 96 (2014).
- ⁶A. Augusto, S. Y. Herasimenna, R. R. King, S. G. Bowden, and C. Honsberg, *J. Appl. Phys.* **121**, 205704 (2017).
- ⁷K. Masuko, M. Shigematsu, T. Hashiguchi, D. Fujishima, M. Kai, N. Yoshimura, T. Yamaguchi, Y. Ichihashi, T. Mishima, N. Matsubara, T. Yamanishi, T. Takahama, M. Taguchi, E. Maruyama, and S. Okamoto, *IEEE J. Photovoltaics* **4**, 1433 (2014).
- ⁸D. Adachi, J. L. Hernández, and K. Yamamoto, *Appl. Phys. Lett.* **107**, 233506 (2015).
- ⁹K. Yoshikawa, W. Yoshida, T. Irie, H. Kawasaki, K. Konishi, H. Ishibashi, T. Asatani, D. Adachi, M. Kanematsu, H. Uzu, and K. Yamamoto, *Sol. Energy Mater. Sol. Cells* **173**, 37 (2017).
- ¹⁰K. Yoshikawa, H. Kawasaki, W. Yoshida, T. Irie, K. Konishi, K. Nakano, T. Uto, D. Adachi, M. Kanematsu, H. Uzu, and K. Yamamoto, *Nat. Energy* **2**, 17032 (2017).
- ¹¹S. Tohoda, D. Fujishima, A. Yano, A. Ogane, K. Matsuyama, Y. Nakamura, N. Tokuoka, H. Kanno, T. Kinoshita, H. Sakata, M. Taguchi, and E. Maruyama, *J. Non-Cryst. Solids* **358**, 2219 (2012).
- ¹²A. Augusto, E. Looney, C. del Cañizo, S. G. Bowden, and T. Buonassisi, *Energy Procedia* **124**, 706 (2017).
- ¹³H. Sai, H. Umishio, T. Matsui, S. Nunomura, T. Kawatsu, H. Takato, and K. Matsubara, *Jpn. J. Appl. Phys., Part 1* **57**, 08RB10 (2018).
- ¹⁴T. Mishima, M. Taguchi, H. Sakata, and E. Maruyama, *Sol. Energy Mater. Sol. Cells* **95**, 18 (2011).
- ¹⁵A. Bianchini, M. Gambuti, M. Pellegrini, and C. Saccani, *Renewable Energy* **85**, 1 (2016).

- ¹⁶J. Haschke, J. P. Seif, Y. Riesen, A. Tomasi, J. Cattin, L. Tous, P. Choulat, M. Aleman, E. Cornagliotti, A. Uruena, R. Russell, F. Duerinckx, J. Champiaud, J. Levrat, A. A. Abdallah, B. Aïssa, N. Tabet, N. Wyrsch, M. Despeisse, J. Szlufcik, S. De Wolf, and C. Ballif, *Energy Environ. Sci.* **10**, 1196 (2017).
- ¹⁷H. Fujiwara and M. Kondo, *J. Appl. Phys.* **101**, 054516 (2007).
- ¹⁸H. Fujiwara and M. Kondo, *Appl. Phys. Lett.* **90**, 013503 (2007).
- ¹⁹S. De Wolf and M. Kondo, *Appl. Phys. Lett.* **90**, 042111 (2007).
- ²⁰W. Liu, F. Meng, X. Zhang, and Z. Liu, *ACS Appl. Mater. Interfaces* **7**, 26522 (2015).
- ²¹K. Ohdaira, T. Oikawa, K. Higashimine, and H. Matsumura, *Curr. Appl. Phys.* **16**, 1026 (2016).
- ²²W. Liu, L. Zhang, R. Chen, F. Meng, W. Guo, J. Bao, and Z. Liu, *J. Appl. Phys.* **120**, 175301 (2016).
- ²³Y. Zhang, C. Yu, M. Yang, L.-R. Zhang, Y.-C. He, J.-Y. Zhang, X.-X. Xu, Y.-Z. Zhang, X.-M. Song, and H. Yan, *Chin. Phys. Lett.* **34**, 038101 (2017).
- ²⁴H. Fujiwara, T. Kaneko, and M. Kondo, *Appl. Phys. Lett.* **91**, 133508 (2007).
- ²⁵K. Ding, U. Aeberhard, F. Finger, and U. Rau, *J. Appl. Phys.* **113**, 134501 (2013).
- ²⁶M. Boccard and Z. C. Holman, *J. Appl. Phys.* **118**, 065704 (2015).
- ²⁷A. Descoedres, L. Barraud, S. De Wolf, B. Strahm, D. Lachenal, C. Guérin, Z. C. Holman, F. Zicarelli, B. Demaurex, J. Seif, J. Holovsky, and C. Ballif, *Appl. Phys. Lett.* **99**, 123506 (2011).
- ²⁸J. Geissbühler, S. De Wolf, B. Demaurex, J. P. Seif, D. T. L. Alexander, L. Barraud, and C. Ballif, *Appl. Phys. Lett.* **102**, 231604 (2013).
- ²⁹J. Shi, M. Boccard, and Z. Holman, *Appl. Phys. Lett.* **109**, 031601 (2016).
- ³⁰L. Zhang, W. Liu, W. Guo, J. Bao, X. Zhang, J. Liu, D. Wang, F. Meng, and Z. Liu, *IEEE J. Photovoltaics* **6**, 604 (2016).
- ³¹S. N. Granata, T. Bearda, F. Dross, I. Gordon, J. Poortmans, and R. Mertens, *Energy Procedia* **27**, 412 (2012).
- ³²D. Deligiannis, R. Vasudevan, A. H. M. Smets, R. A. C. M. M. van Swaaij, and M. Zeman, *AIP Adv.* **5**, 097165 (2015).
- ³³S. De Wolf and M. Kondo, *Appl. Phys. Lett.* **91**, 112109 (2007).
- ³⁴J. P. Seif, B. Niesen, A. Tomasi, C. Ballif, and S. De Wolf, *Appl. Phys. Lett.* **110**, 151601 (2017).
- ³⁵Z. C. Holman, A. Descoedres, L. Barraud, F. Z. Fernandez, J. P. Seif, S. De Wolf, and C. Ballif, *IEEE J. Photovoltaics* **2**, 7 (2012).
- ³⁶R. Sinton and A. Cuevas, in *Proceedings of 16th Eur. Photovolt. Sol. Energy Conf.*, Glasgow (2000), pp. 1–4.
- ³⁷S. Nunomura and M. Kondo, *Appl. Phys. Lett.* **93**, 231502 (2008).
- ³⁸W. Beyer, in *Thin Film Silicon Sol. Cells*, edited by A. Shah (EPFL Press, Lausanne, 2010), pp. 64–76.
- ³⁹M. H. Brodsky, M. Cardona, and J. J. Cuomo, *Phys. Rev. B* **16**, 3556 (1977).
- ⁴⁰G. Lucovsky, *Sol. Cells* **2**, 431 (1980).
- ⁴¹A. A. Langford, M. L. Fleet, B. P. Nelson, W. A. Lanford, and N. Maley, *Phys. Rev. B* **45**, 13367 (1992).
- ⁴²A. H. M. Smets, W. M. M. Kessels, and M. C. M. van de Sanden, *Appl. Phys. Lett.* **82**, 1547 (2003).
- ⁴³S. Shimizu, M. Kondo, and A. Matsuda, *J. Appl. Phys.* **97**, 033522 (2005).
- ⁴⁴T. Matsui, H. Sai, K. Saito, and M. Kondo, *Prog. Photovoltaics* **21**, 1363 (2013).
- ⁴⁵S. Nunomura, I. Sakata, and K. Matsubara, *Appl. Phys. Express* **10**, 081401 (2017).
- ⁴⁶J. Müllerová, P. Šutta, G. van Elzakker, M. Zeman, and M. Mikula, *Appl. Surf. Sci.* **254**, 3690 (2008).
- ⁴⁷J. Haschke, O. Dupré, M. Boccard, and C. Ballif, *Sol. Energy Mater. Sol. Cells* **187**, 140 (2018).
- ⁴⁸D. Zhang, A. Tavakoliyaraki, Y. Wu, R. A. C. M. M. van Swaaij, and M. Zeman, *Energy Procedia* **8**, 207 (2011).
- ⁴⁹F. Haase, S. Schafer, C. Klamt, F. Kiefer, J. Krugener, R. Brendel, and R. Peibst, *IEEE J. Photovoltaics* **8**, 23 (2018).
- ⁵⁰N. Jensen, U. Rau, R. M. Hausner, S. Uppal, L. Oberbeck, R. B. Bergmann, and J. H. Werner, *J. Appl. Phys.* **87**, 2639 (2000).
- ⁵¹K. Watanabe, N. Matsuki, and H. Fujiwara, *Appl. Phys. Express* **3**, 116604 (2010).
- ⁵²A. Richter, M. Hermle, and S. W. Glunz, *IEEE J. Photovoltaics* **3**, 1184 (2013).
- ⁵³H. Sai, T. Matsui, K. Saito, M. Kondo, and I. Yoshida, *Prog. Photovoltaics* **23**, 1572 (2015).
- ⁵⁴J. Peter Seif, A. Descoedres, M. Filipič, F. Smole, M. Topič, Z. Charles Holman, S. De Wolf, and C. Ballif, *J. Appl. Phys.* **115**, 024502 (2014).
- ⁵⁵A. Paduthol, M. K. Juhl, G. Nogay, P. Löper, and T. Trupke, “Measuring carrier injection from amorphous silicon into crystalline silicon using photoluminescence,” *Prog. Photovoltaics* **238** (published online, 2018).